High strength, low stiffness, porous NiTi with superelastic properties

Christian Greiner [1], Scott M. Oppenheimer, David C. Dunand *

Department of Materials Science and Engineering, Northwestern University, Evanston, IL 60208, USA

Abstract

Near-stoichiometric NiTi with up to 18% closed porosity was produced by expansion at 1200 °C of argon-filled pores trapped by powder metallurgy within a NiTi billet. When optimally heat-treated, NiTi with 6–16% porosity exhibits superelasticity, with recoverable compressive strains up to 6% at a maximum compressive stress up to 1700 MPa. The apparent Young's modulus of NiTi with 16% porosity, measured during uniaxial compression, is in the range of 15–25 GPa (similar to human bone), but is much lower than measured ultrasonically (~40 GPa), or predicted from continuum elastic mechanics. This effect is attributed to the reversible stress-induced transformation contributing to the linear elastic deformation of porous NiTi. The unique combination of low stiffness, high strength, high recoverable strains and large energy absorption of porous superelastic NiTi, together with the known biocompatibility of NiTi, makes this material attractive for bone–implant applications.
© 2005 Acta Materialia Inc. Published by Elsevier Ltd. All rights reserved.

Keywords: Nickel; Titanium; Nitinol; Foams; Superelasticity; Bone replacement

1. Introduction

The Young's moduli of metallic materials used for bone replacement range from ~110 GPa for titanium alloys to ~190 GPa for stainless steel and ~210 GPa for Co-based alloys [1], and are thus much higher than the modulus of human cancellous bone (<3 GPa) or compact bone (12–17 GPa) [2]. This large stiffness mismatch between monolithic metallic implant and the surrounding human bone results in stress-shielding, eventually inducing implant loosening [3]. Reducing the stiffness of metallic implants can be achieved by adding porosity uniformly within the implant, since stiffness decreases with the square of porosity in porous and cellular materials [2]. Currently, surface porosity is produced on monolithic implants to improve anchorage of bone [1,4,5], but with minimal reduction of implant stiffness. By contrast, a fully porous prosthetic material can decrease stiffness and the stress-shielding effect while also, if appropriate pore size and connectivity are achieved, allowing bone ingrowth, thus improving the strength of the implant/bone interconnection [6,7].

Porous materials made from bio-compatible metals have been demonstrated for stainless steel [8], titanium [8,9] and tantalum [10]. Near-stoichiometric nickel–titanium alloys (abbreviated as NiTi in the following) are particularly promising for such applications, as they exhibit proven biocompatibility [6,11] and the lowest stiffness of any bio-compatible metals (55–80 GPa, depending on temperature, for austenitic NiTi [12]). It should thus be possible to match the stiffness of human bone with porous NiTi at porosity levels that are much lower than those needed for the other bio-compatible metals [7]. This is desirable, since strength (in particular fatigue strength) also decreases more than linearly with porosity in porous metals [2]. A further interesting

* Corresponding author. Tel.: +1 847 491 5370.
E-mail address: dunand@northwestern.edu (D.C. Dunand).
[1] Present address: Max Planck Institute for Metals Research, Heisenbergstr. 3, D-70569 Stuttgart, Germany.

mechanical property of nickel-rich NiTi is superelasticity, enabling monolithic NiTi to recover up to 8% strain in uniaxial deformation by a reversible stress-induced transformation [13]. Human bone also recovers high strains (up to 2% [2]) and NiTi can thus match this mechanical property as well.

One of the simplest processing approaches to create porous NiTi consists of mixing elemental nickel and titanium powders with a blowing agent, e.g., TiH_2 [17]. At high temperature, the metallic powders in the pressed preform react exothermally while the hydride decomposes and releases hydrogen. The resulting material has a mostly open porosity of 30–40%, [17,18]. Numerous phases coexist with NiTi, i.e., the intermetallics Ni_3Ti, Ti_2Ni and elemental Ti and Ni (a strong allergen) [19,20]. Some superelastic behavior is measured in these foams, with failure occurring in mixed cleavage and ductile fracture mode [17,18]. Recently, it was demonstrated that a slow heating to 1150 °C at 1 °C/min could result in complete homogenization of these undesirable phases [21].

When a pressed pellet of mixed Ni and Ti powders is heated and ignited at one edge [14,15,22–28], porous NiTi is created in a reaction wave propagating traveling through the pellet through self-propagating high-temperature synthesis (SHS), as previously studied for numerous other intermetallics [29]. Mostly-open porosity in the range 45–65% is achieved, with a 120–600 μm pore size. Upon implantation in animals, bone ingrowth within these porous NiTi samples was reported [11,30]. While the SHS method is very rapid and energy-efficient, it suffers from lack of control with respect to pore size, pore volume fraction, and chemical homogeneity: Ti_2Ni, Ni_3Ti and Ni_4Ti_3 are almost always observed, with a corresponding embrittling effect. Some studies [25,31] report superelastic behavior of the foams in compression, but stresses are low due to the high porosity. Lagoudas and Vandygriff [32] added argon gas to canisters containing Ni and Ti powders. SHS processing in a pressurized hot-isostatic press (HIP) and subsequent annealing at 900 °C allowed the argon to expand and form large-scale porosity (42–50%), but with residual Ni_3Ti and $NiTi_2$ phases. Porous samples exhibited superelasticity, with however partial strain recovery on unloading and microcracking [32,33].

In a different approach, Zhao et al. [34] produced NiTi with 13% and 25% porosity through spark plasma sintering of pre-alloyed NiTi powders. The 25% porosity material was found to be very weak, due to formation of undesirable intermetallics and incomplete bonding between powders. One superelastic loop was measured for the 13% porosity sample, where a maximum compressive stress of 950 MPa induced a strain of 4.6% which was fully recovered superelastically on unloading.

In a recently published short communication [16], we fabricated porous NiTi by the gas expansion method,

previously used to produce titanium and Ti–6Al–4V foams with up to 40% porosity [9,35–37]. First, pressurized Ar bubbles are created by HIP densification of pre-alloyed NiTi powders together with Ar gas; second, these bubbles are expanded by exposure of the billet to high temperature and low pressure. After heat-treatment, NiTi with 17% closed pores was superelastic (recovering 7% strain in uniaxial compression after a maximum stress of 825 MPa) and very compliant (apparent elastic modulus of 9 GPa). This combination of low stiffness, high strength, and high recoverable strains makes such material ideal for bone implants.

The purpose of the present paper is to systematically study porous NiTi produced by the above gas expansion method [16]. We report here kinetics of pore expansion in NiTi for various argon pressures and the mechanical properties (stiffness, strength and superelastic recovery) of porous NiTi with a range of porosities, subjected to various heat-treatments designed to induce or suppress the superelastic effect.

2. Experimental procedures

The fabrication process is shown in Fig. 1: pre-alloyed martensitic NiTi powders (Ni–50.6at.%Ti, 99.9% purity, size between 44 and 177 μm, from Specialty Metals Corp., NY) were mixed with small quantities of elemental nickel powders (99.9% purity, size between 44 and 177 μm), for an overall composition of Ni–49.0at.%Ti. Such nickel-rich NiTi alloys are known to exhibit superelastic behavior at room temperature [13], and a monolithic billet of the same composition fabricated with the same NiTi–Ni powders was found in previous studies to exhibit superelastic behavior in compression [38–40]. The mixed powders were filled in two mild-steel cans with an outer diameter of 35.0 mm and a wall thickness of 1.6 mm, which were evacuated and backfilled with argon. Two samples, labeled A and B in the following, were created with initial Ar pressures of 207 and 449 kPa (about 2 and 4.5 atm), respectively. The sealed cans were densified by HIP at 1066 °C under a pressure of 103 MPa for 4 h at UltraClad Corp. (Andover, MA). Electro-discharge machining was used to cut cubic samples ($6.0 \times 6.0 \times 6.0$ mm^3), originating from the center of the billets; for the A billet only, rectangular samples ($5.0 \times 5.0 \times 10.0$ mm^3) were also machined from a region closer to the edges of the billets. A control sample was taken from an Ar-free NiTi billet of the same composition previously produced by the same HIP technique, except for the lack of Ar [40].

All samples were lightly polished with 600 grit SiC paper to remove any contamination from machining. Foaming experiments were performed using rectangular A and cubic B specimens at 1200 °C under high vacuum ($<10^{-5}$ Torr) for times as long as 200 h. At
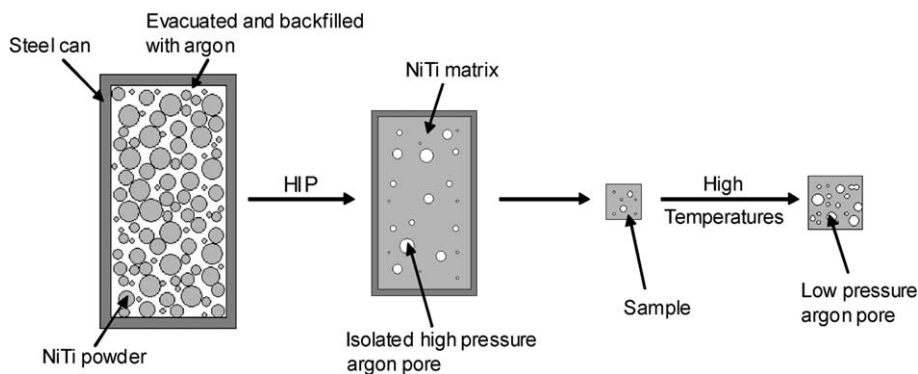
Fig. 1. Schematic of foaming process for NiTi: argon gas is trapped within the metal during HIP powder compaction and subsequently expanded at high temperatures and low pressure.

regular intervals, foaming was interrupted and the sample density was measured by the Archimedes method in deionized water, after coating with a thin layer of vacuum grease to prevent water penetration in open pores.

Metallographic examination was done by optical and scanning electron microscopies on mounted samples which were ground and polished to 0.05 μm alumina, to assess pore size (by manual line intercept) as well as pore spatial distribution and morphology (by qualitative observation). For as-HIPed A and B materials, metallographic samples originated from the billet edge, while for foamed materials, a rectangular A sample with 18.8% porosity was used.

The dynamic Young's modulus was determined from sound velocity measurements in longitudinal and transversal directions using the ultrasonic pulse-echo-method for one control monolithic sample (0% porosity) and five A samples with the following porosities: $0.60 \pm 0.06\%$, $2.3 \pm 0.1\%$, $5.6 \pm 0.1\%$, $11.0 \pm 0.1\%$ and $17.7 \pm 0.1\%$. The first sample was in the as-HIPed condition, and the last four samples were foamed at 1200 °C for 0, 0.08, 5 and 170 h, respectively (where time does not include the heating and cooling ramps, e.g., the 0 h foamed sample was cooled immediately upon reaching 1200 °C).

Uniaxial compression testing was performed on rectangular A samples with four different porosities (monolithic, 5.6%, 11% and 16%) and three different thermal histories: (i) furnace cooling (as-foamed); (ii) homogenization (4 h at 1000 °C in vacuum, quenched in ambient-temperature brine); (iii) homogenization (as above) followed by aging (4 h at 400 °C in air, quenched in ambient-temperature water). The furnace-cooled samples experienced a variable cooling rate ranging from ~3 K/s near 1200 °C to ~0.01 K/s near ambient temperature, as shown in Fig. 2. Compression tests were carried out at ambient temperature (23 °C) at initial strain rates <0.01 min^{-1}, low enough to eliminate any temperature effect from the latent heat of transformation [38]. A self-aligning compression cage was used to
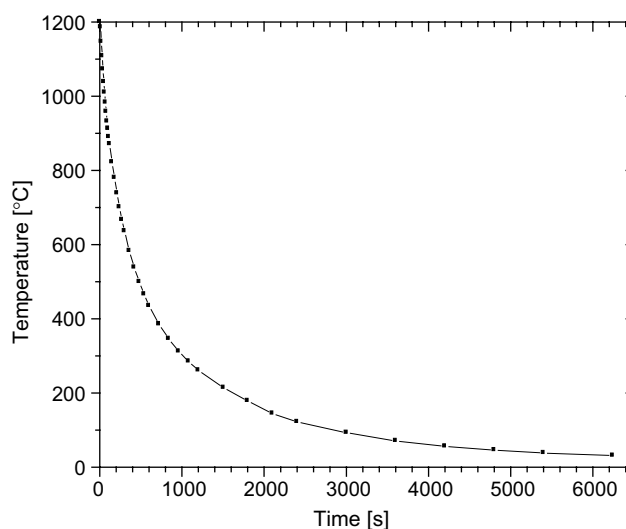

Fig. 2. Cooling curve for furnace-cooled NiTi porous samples.

assure uniaxial deformation, and strain was measured by laser extensometry. At 100 MPa stress intervals, the load was reduced to near zero before being increased again, resulting in multiple load–unload loops.

3. Results

3.1. Foaming kinetics and microstructures

The initial porosity of the as-HIPed A and B materials was determined by the Archimedes method as $0.60 \pm 0.06\%$ and $1.16 \pm 0.05\%$, respectively, using a density value of 6.5057 ± 0.0020 g/cm^3 for pore-free NiTi (as measured on the pore-free control sample, and in good agreement with literature data [12]). Line-intercept measurements on SEM micrographs of polished cross-sections yielded an average pore size of 4.6 ± 2.2 μm and 4.1 ± 3.0 μm for A and B materials, respectively. A representative SEM micrograph for as-HIPed B material is shown in Fig. 3(a).
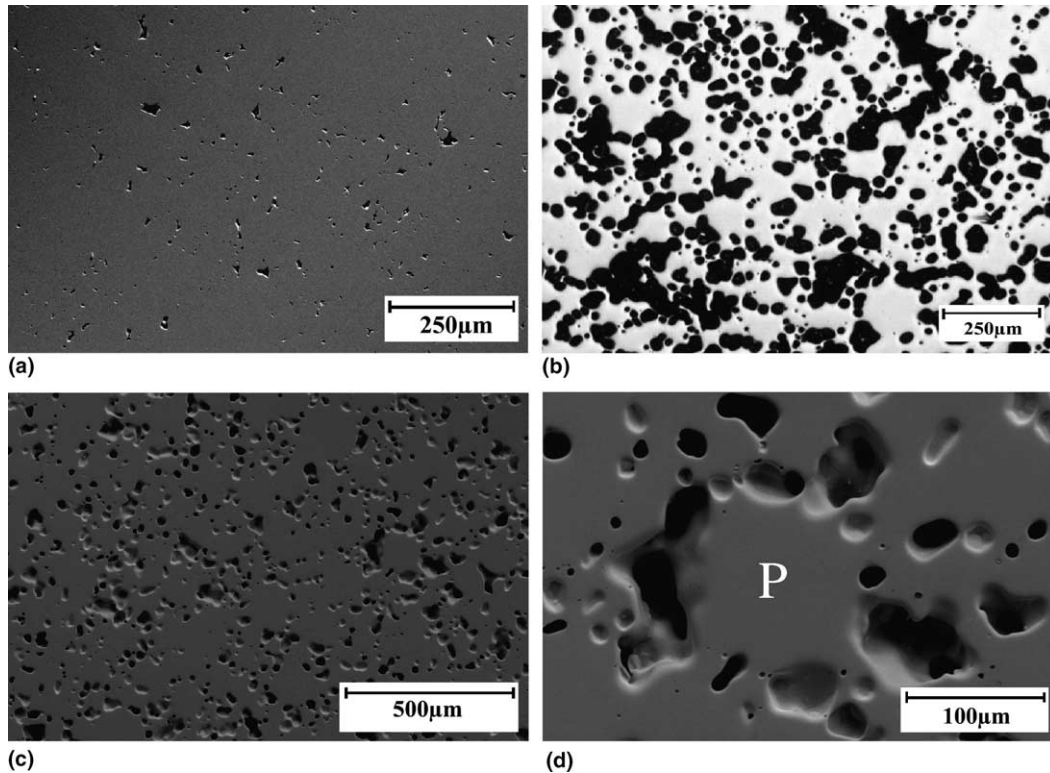
Fig. 3. (a) SEM micrograph of as-HIPed B material; (b) optical micrograph of 18.8% porous A material; (c) SEM micrographs of 18.8% porous A material; (d) high-magnification detail of (c), showing a rounded prior NiTi particle (P) surrounded by a network of merged pores.

Fig. 3(b) shows an optical micrograph for the polished cross-section of an A sample with a porosity of $18.8 \pm 0.1\%$, after foaming for 200 h at 1200 °C. Fig. 3(c) provides a corresponding SEM picture with enhanced depth of field, and Fig. 3(d) presents a higher magnification SEM picture illustrating pore clustering around a primary powder particle. Line-intercept measurements on the SEM micrographs yielded an average pore size of 21 ± 5 µm.

Foaming curves for A and B materials are plotted in Fig. 4 as total sample porosity vs. total foaming time at 1200 °C (i.e., discounting heating and cooling times). For each material, two samples were foamed, as illustrated by open and closed data points in Fig. 4, which shows that excellent reproducibility was achieved. As expected, samples A, with about half the argon backfill pressure of samples B, foam at a slower rate. For the two cubic B samples, the three edge dimensions were monitored during foaming, and isotropic expansion (with no face bulging) was observed, indicating isotropic pore growth. This is confirmed by micrographs of cross-sections showing no preferred direction for pore growth or coalescence.

3.2. Mechanical testing

Engineering stress–strain plots are presented in Fig. 5(a)–(c) for monolithic samples in the furnace
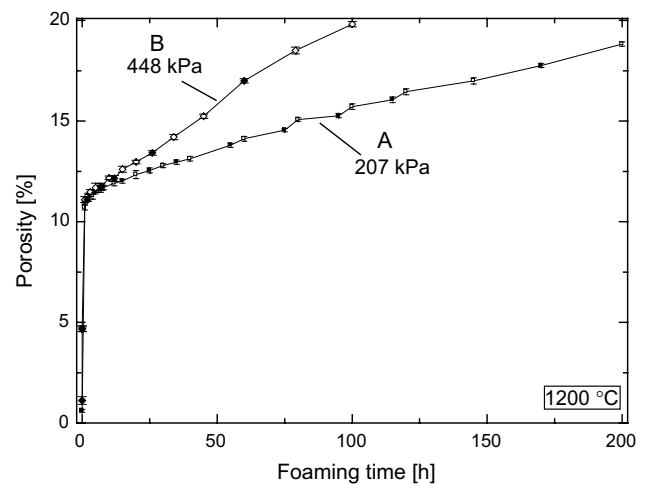

Fig. 4. Total porosity as a function of time during isothermal foaming at 1200 °C for A and B materials (207 and 448 kPa, respectively). Data points for each curve originate from two samples, identified by open and closed symbols.

cooled, homogenized and aged states, respectively, and in Fig. 5(d)–(f) for foamed samples with the highest porosity (16%) in the same three states. It is apparent that the heat-treatment has a strong effect on the stress–strain curves for both monolithic and porous samples.

For monolithic NiTi in the furnace-cooled condition (Fig. 5(a)), the loading curve envelope is characterized
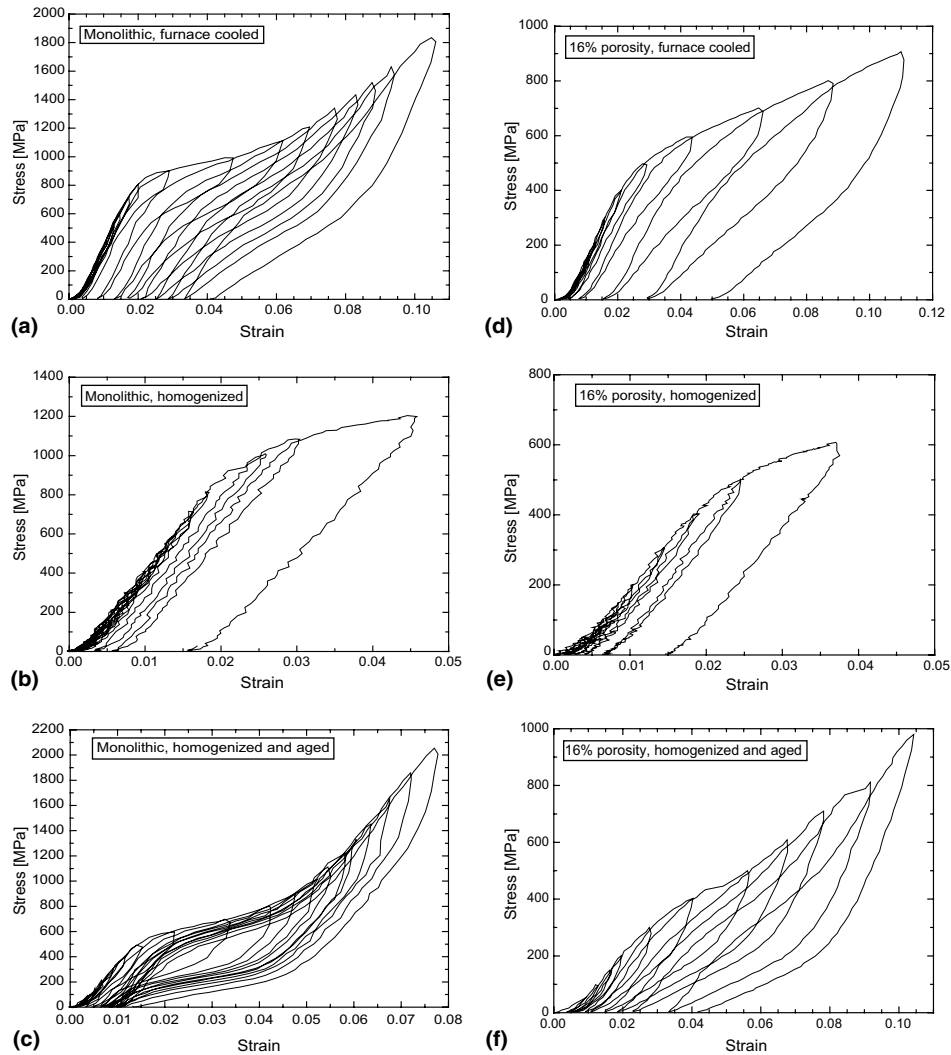
Fig. 5. Compressive stress–strain curves as a function of heat-treatment and porosity. Monolithic samples: (a) furnace cooled; (b) homogenized; (c) aged. Porous samples (16%): (d) furnace cooled; (e) homogenized; (f) aged.

by a yield stress of about 850 MPa (with a corresponding strain of 2%), a plateau where stress increases slowly with strain up to about 7%, followed by a more rapid stress increase up to the maximum tested value of 1800 MPa. Unloading curves exhibit partial non-linear recovery of the strain, while reloading curves follow the same trajectory as the envelope curve. This mechanical behavior is typical of partially superelastic NiTi [13]. When the furnace-cooled sample is homogenized (Fig. 5(b)), the stress–strain curve is characterized by a yield stress at about 950 MPa, followed by strain hardening up to the highest tested stress of 1200 MPa. All unloading and reloading curves are linear. The overall behavior is typical of an elastic–plastic material, without superelasticity, as expected from the annealing treatment. Finally, the NiTi sample aged after homogenization shows a fully superelastic behavior (Fig. 5(c)), similar in nature to that of the furnace-cooled sample, except for the lower yield stress (about 550 MPa) and

shorter plateau (about 5% total strain), and for more completely recovered strains (up to about 7%) on unloading. Very similar stress–strain curves for superelastic NiTi are reported in the literature [13].

As for the monolithic samples, the 16% porous samples are sensitive to heat-treatment. In the furnace-cooled condition (Fig. 5(d)), partial superelasticity is observed, with a yield stress of about 450 MPa, about half the value of 850 MPa for the monolithic specimen. Strain recovery in the last unloading curve is similar for both materials (about 6% strain recovered from a maximum strain of 11%). After annealing the 16% porous sample, superelasticity disappears (Fig. 5(e)), as for the monolithic sample (Fig. 5(b)), and the mechanical behavior is elasto-plastic, with a yield stress of about 450 MPa, about half that of monolithic NiTi. Finally, after aging, the 16% porous material becomes superelastic (Fig. 5(f)), like the monolithic material (Fig. 5(c)). The loading envelope is characterized by a first
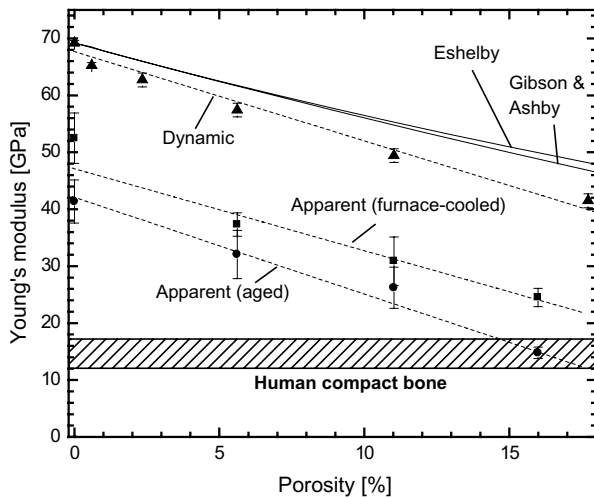
Fig. 6. Effect of porosity on Young's modulus for various heat-treatments. The experimental data for the dynamic and the apparent Young's moduli is compared to Eshelby model predictions for porous solids and to a model by Gibson and Ashby.

near-linear region (up to about 300 MPa, again about half the value for monolithic NiTi), with an apparent modulus of about 14 GPa (as compared to 46 GPa for monolithic NiTi). A second near-linear region extends to about 800 MPa, with a slope of 7 GPa (similar value to that of monolithic NiTi). For the porous sample, superelastic recovery strains are improved after annealing as compared to the furnace-cooled samples, but less so than for the monolithic sample.

For superelastic monolithic NiTi, it is difficult to determine the true Young's modulus from macroscopic stress–strain curves, since deformation in the initial linear region usually contains both elastic and superelastic contributions [41]. The apparent Young's moduli for the monolithic NiTi samples (as determined by a best-fit line through the stress–strain curve) are in the range $E_{app} = 41–52$ GPa, depending on heat-treatment. These values are significantly lower than the dynamic value $E_{dyn} = 69.5$ GPa determined ultrasonically, which is within the broad literature range of 55–80 GPa [12]. A similar discrepancy between apparent and dynamic Young's moduli is found for the porous samples, as illustrated in Fig. 6 where E_{app} and E_{dyn} are plotted as a function of porosity. This plot shows that both the dynamic and apparent Young's moduli decrease near linearly with porosity, and that the heat-treatment affects the apparent modulus, with the aged samples displaying a significantly lower modulus than the furnace-cooled samples.

4. Discussion

4.1. Microstructure

After HIP compaction, the B material has a porosity $(1.16 \pm 0.05\%)$ which is, within experimental error,

twice that of the A material $(0.60 \pm 0.06\%)$, as expected from the approximate doubling in initial argon backfill pressures (from 207 to 448 kPa). Because the average pore sizes for both as-HIPed A and B materials are the same (within a broad error range), it can be concluded that increasing the backfill pressure increases the pore number density rather than their size. It is apparent from Fig. 3(a) that the pore spatial distribution is not random, but that pores are located around the prior NiTi powder particles, which can be identified as pore-free circular regions. The pore shape is generally rounded, with some pores being more elongated; both shapes are generally free of cusps, indicative of extensive plastic flow during NiTi powder HIP densification.

As expected from the non-random initial porosity distribution, porosity is not evenly distributed after foaming to 18.8%, as shown in Fig. 3(b) and (c) where many rounded, pore-free regions corresponding to prior NiTi particles are visible. Such a particle is shown in Fig. 3(d), surrounded by pores which have grown and merged with each other during the foaming stage. Occasionally, a high number of pores coalesced to form sinuous, highly elongated voids (visible in Fig. 3(b) and (c)), as also observed in similar foaming experiments performed on titanium [42,43]. Overall, the pore shape is smooth, as expected from the pore expansion process and the lack of extensive pore wall fracture.

The pore size for cancellous bone is in the 1–100 μm range and artificial porous bone substitution materials usually have pore sizes between 100 and 500 μm [1]. For the present porous NiTi materials, the merged pores are near the bottom of the latter size range, but the individual unmerged pores are much smaller, about 10–20 μm. Furthermore, porosity is closed, thus precluding bone ingrowth upon foam implantation. However, for titanium foamed by the same isothermal argon expansion method, open pores with 75–250 μm size were achieved, with porosities in the range 20–30% [9,42]. A similar level of porosity with larger pores open to the specimen surface should be achievable for NiTi if foaming parameters are adjusted, e.g., by using longer times, higher temperatures and/or higher argon pressures, as discussed in the following section.

4.2. Pore expansion process

Foaming curves for A and B materials (Fig. 4) show very rapid foaming up to a porosity of 11%, followed by a much slower, near-linear increase, with a slope that is twice as high for material B than for material A, as expected from their respective Ar backfill pressures. A similar trend of faster foaming with increased Ar content was reported for Ti–6Al–4V [37].

It is apparent from Fig. 4 that further foaming could occur if longer times were used, thus indicating that significant gas pressure remains in the pores. For the B

sample shown in Fig. 3(a), foaming resulted in a porosity increase from 0.6% to 19% after 100 h at 1200 °C, and a pore size increase from $4.1 \pm 3.3 \, \mu m$ to $21 \pm 5 \, \mu m$. Mass conservation links the initial and final porosity f_i and f_f with initial and final pore radius r_i and r_f as:

$$\frac{r_f}{r_i} = \left(\frac{f_i^{-1} - 1}{f_f^{-1} - 1}\right)^{1/3} \tag{1}$$

under the simplifying assumptions that pores are spherical and mono-sized. Inserting $f_i = 0.006$ and $f_f = 0.19$ in Eq. (1), a pore radius ratio $r_f/r_i = 3.4$ is predicted, which is in reasonable agreement with the experimental value of $21/4.1 = 5.1$ given that r_i has a large error range and that the experimental diameter values are for average cross-sections of spheroidal pores, many of which have merged. The pore pressure ratio is expected to vary by a factor $(r_f/r_i)^3 = 39$, at constant temperature. Then, assuming that the internal pore pressure at the HIP temperature is equal to the external HIP pressure (103 MPa), the final pore pressure for $f_f = 0.19$ at the foaming temperature is $103/39 = 2.6$ MPa (neglecting the small difference between HIP and foaming temperatures). It is thus apparent that, for the 19% porous B sample, there is considerable gas pressure for further pore expansion. Porosities as high as 85% could be reached if pores were to expand until their internal pressure is 0.1 MPa (Eq. (1)). As observed in Refs. [9,36,42–44] for titanium foams, such high porosities are not achieved, because pores merge with each other and connect to the sample surface, so that argon gas escapes prematurely; for titanium foams, a porosity as high as 30% was achieved under isothermal creep conditions (similar to those used here for NiTi) and 44% under superplastic conditions [42,43].

Previous research on titanium isothermal foaming indicates that foaming rates are very sensitive to powder size and size distribution. For the same foaming temperature of 960 °C and initial Ar backfill pressure of 330 kPa, a porosity of 20% is reached in as little as 0.5 h (using unsieved powders with size below 150 µm) [9] or as long as 100 h (using sieved powders with 62–88 µm size range) [42]. For comparison, the present B NiTi materials (with sieved powders) reached this porosity after 100 h, but at significantly higher temperature of 1200 °C and backfill pressure of 448 kPa. NiTi, because of its higher creep resistance as compared to unalloyed titanium, should indeed exhibit slower foaming kinetics at the same gas pressure and temperature. Further evidence of the slow rate of foaming for NiTi is given by the report by Kearns et al. [37] who achieved porosities as high as 32% for Ti–6Al–4V with an argon backfill pressure of 100 kPa after foaming at 1240 °C for 10 h, as compared to 12% for NiTi for the same time and similar temperature (but higher gas pressure).

4.3. Mechanical properties

4.3.1. Stiffness

Fig. 6 shows that the dynamic Young's modulus E_{dyn} is always significantly higher than the apparent moduli E_{app}. The true Young's modulus is expected to be represented by E_{dyn}, since the ultrasound method produces infinitesimal strains that remain in the linear elastic range, even for NiTi which can exhibit transformation strains at very low applied stress. By contrast, E_{app} is determined as the best-fit slope of the linear part of the stress–strain curves over a large stress range, so that small superelastic strains, due to the onset of the reversible stress-induced transformation in a subset of optimally oriented grains, can result in a low value of the apparent Young's modulus. Since the critical stress for the stress-induced transformation is sensitive to thermal history, the apparent Young's modulus is expected to vary with heat-treatments, as indeed shown in Fig. 6: for all porosity values (including 0%), E_{app} is significantly lower (by about 8 GPa) for the aged than for the furnace-cooled samples. This trend may be explained by the fact that the aged samples have the highest propensity for large-scale superelasticity (Fig. 5(d) and (f)). For bio-medical implants, stiffness is better described by E_{app} than E_{dyn}, due to the relatively high stresses and strains expected in this application.

The Young's modulus of porous metals can be modeled with the Eshelby technique, assuming that pores are spherical (or ellipsoidal) and uniformly distributed within the matrix. The Eshelby predictions are shown in Fig. 6, using the measured value $E_{NiTi} = 69.5$ GPa and a Poisson's ratio $\nu_{NiTi} = 0.33$ [12], and are overpredicting the measured values for E_{dyn} by up to 15%. The discrepancy is not surprising, given the inhomogeneous distribution of pores and their non-spherical shapes. The same magnitude of overprediction between measurements and model predictions has also been found for titanium foams manufactured using the same solid-state foaming method [45]. We also consider a widely used model by Gibson and Ashby, which predicts that the Young's modulus of a foam decreases with the square of its porosity [2]. This model can be derived theoretically assuming strut bending in cellular structures with high porosity (above ~75%) but has been found to hold empirically to much lower porosity. The model predictions are plotted in Fig. 6 and found to follow, to a very good approximation, the Eshelby predictions up to the highest porosity studied here (18%).

The apparent Young's modulus for the sample with 16% porosity in the aged condition, $E_{app} = 15 \pm 1$ GPa, is in the range displayed by wet compact human bone, $E_{bone} = 12$–17 GPa. Thus, to achieve the goal of avoiding stress-shielding by matching the implant modulus with that of bone, it may be sufficient to foam NiTi in the relatively modest porosity range 15–20%, provided

the correct heat-treatment producing superelasticity (leading to $E_{app} \ll E_{dyn}$) is used. By comparison, porous superelastic NiTi produced by SHS was found to display $E_{app} = 15$ GPa at a much higher porosity of 42% [32].

4.3.2. Stress–strain curves

Comparison of Fig. 5(b) and (c) clearly demonstrates that, for monolithic NiTi, superelasticity is not active after a homogenization heat-treatment, but is restored by a subsequent aging treatment. This well-known effect is explained by the dissolution of fine, nanoscale precipitates during homogenization, thus allowing the easy motion of dislocations [13]. Subsequent annealing leads to the formation of these precipitates, which, by blocking dislocation glide, allow for the activation of stress-induced transformation, responsible for the superelastic effect [13]. The partial superelasticity exhibited by the furnace-cooled sample (Fig. 5(a)) indicates that precipitates were formed during the relatively slow cooling occurring in the furnace (Fig. 2).

The 16% porous NiTi samples exhibit qualitatively the same behavior as the monolithic samples: partial superelasticity upon furnace cooling (Fig. 5(d)), no superelasticity after homogenization (Fig. 5(e)), and extensive superelasticity after annealing (Fig. 5(f)). To the best of our knowledge, there is no report on compression tests for porous NiTi showing room-temperature superelasticity at the very high stresses (900–1000 MPa) studied here. Also noteworthy is the lack of microcracking, despite the high stresses and

strains achieved here, which was reported for 42% porous NiTi produced by combustion synthesis [32].

The effect of heat-treatment on the stress–strain behavior of the monolithic and 16% porous materials is illustrated in Fig. 7(a) and (d), where the last load–unload loops from Fig. 5(a)–(f) are plotted after shifting to the origin to ease comparison. In effect, the prior loops shown in Fig. 5(a)–(f) can be considered as training cycles, which are known in monolithic samples to improve superelasticity [13]. Similar graphs are shown for the samples with 5.6% and 11% porosity in Fig. 7(b) and (c). It is apparent from Fig. 7(a)–(d) that aging reduces the width of the load–unload hysteresis as compared to furnace cooling. The aged samples show a lower stress plateau (i.e., undergo superelastic deformation at lower stresses) but exhibit higher stresses at large strain, leading to a cross-over of the two loading curves in Fig. 7(a)–(d). While a prediction of porous sample stress–strain curves from the knowledge of the behavior of the monolithic sample will require extensive micromechanical modeling taking into account stress concentration and multiaxiality near the pores, it is qualitatively apparent that the relative shapes for the curves of the aged and furnace-cooled monolithic samples (Fig. 7(a)) carry over to the porous samples (Fig. 7(b)–(d)).

Comparison between Fig. 5(a), (c) and (d), (f) indicates that, for a given nominal stress, the 16% porous samples exhibit larger recoverable (elastic and superelastic) strains and larger non-recoverable (plastic) strains than the
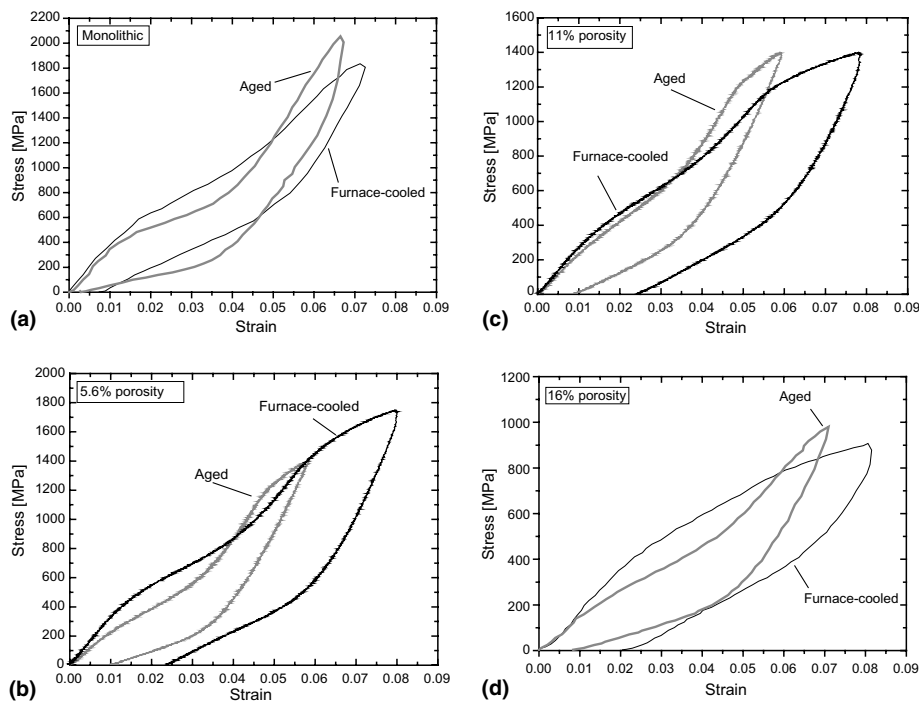

Fig. 7. Comparison of compressive stress–strain curves for furnace cooled and aged states: (a) monolithic (last loop from Fig. 5(a) and (c)); (b) 5.6% porosity; (c) 11% porosity; (d) 16% porosity (last loop from Fig. 5(d) and (f)).
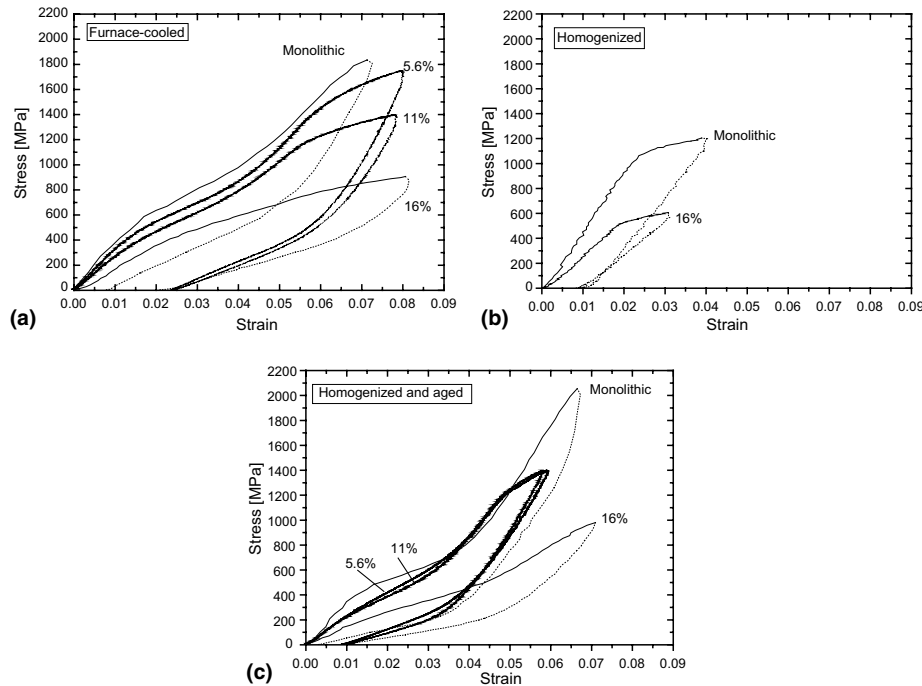
Fig. 8. Comparison of compressive stress–strain curves for NiTi with 0%, 5.6%, 11% and 16% porosity for various heat-treatments: (a) furnace cooled; (b) homogenized: (c) aged.

monolithic samples, for both furnace cooled and aging heat-treatments. Equivalently, for a given recoverable strain, the stress for the porous sample is lower (by about a factor 2) than for the monolithic sample.

Fig. 8(a)–(c) show the last load–unload loops of the monolithic and porous samples for each of the three heat-treatments. These comparisons indicate that the yield stress and apparent Young's modulus decrease with porosity in a monotonic manner (with the exception of the aged samples with 5.6% and 11% porosity which have overlapping curves). On unloading for the furnace cooled and aged states, all three porous samples exhibit the same recoverable strain (about 5.5%), which is only slightly below that measured on the monolithic samples (6%). The unrecoverable plastic strain is therefore larger for the porous samples, especially for the furnace-cooled ones, in part because they were strained to larger values. Again, detailed micromechanical modeling of the type performed for porous titanium deforming by slip only [46] will be needed to quantify the effect of stress concentration on the strains produced by stress-induced transformation and dislocation glide; however, it is apparent from the present study that porous NiTi retains most of its superelastic strain recovery capability.

4.3.3. Energy absorption

Using porous NiTi in energy management and vibration control applications (including bone implants) is promising, due to very high damping coefficient of superelastic, monolithic NiTi and the high mechanical energy it can absorb and dissipate during mechanical loading–unloading loops [13]. The maximum energy E_{max} absorbed by the monolithic and porous samples was determined by calculating the area under the loading branch of each of the stress–strain loops for materials in the aged condition (shown in Fig. 5(c) and (f) for the 0% and 16% porosity samples). Fig. 9(a) and (b) show plots of E_{max} (expressed in MJ/m^3) as a function of the maximum strain ε_{max} or maximum stress σ_{max} for each mechanical loop.

In Fig. 9(a) where the energy is plotted as a function of the maximum loop strain, the energy decreases with increasing porosity, the drop being modest up to 11% porosity but much larger (by about a factor 2) for 16% porosity, as a result of the lower stresses achieved by that sample at a given strain. Thus, for displacement-controlled applications, the monolithic and 5.6% porosity materials are most favorable in terms of energy absorption per sample volume. Expressing the energy per unit mass (MJ/kg), does not alter significantly this conclusion, given the relatively modest porosity levels. An example for such a strain-controlled application is energy management during an earthquake, where strains of a given amplitude are generated on large structures and must be absorbed by dampers (a fraction of this energy is dissipated in the form of heat and the rest is recoverable during the superelastic unloading).

The picture changes when Fig. 9(b) is considered, where the energy is plotted as a function of maximum
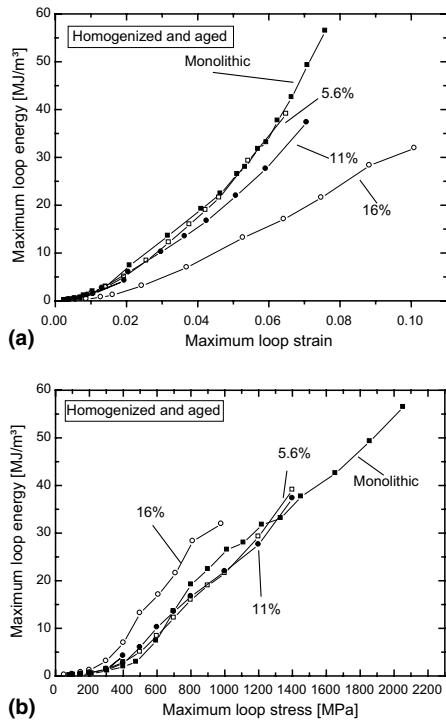
Fig. 9. Maximum energy stored on mechanical loading for NiTi with 0%, 5.6%, 11% and 16% porosity in the aged condition as a function of (a) maximum strain and (b) maximum stress for each mechanical loop.

loop stress. At a given stress, the 16% porous material absorbs more energy than the monolithic and low porosity material, so that in load-controlled applications, the porous material is more favorable. This is the case where shocks are to be absorbed, e.g., for packaging applications or bone implants (as a result of physical activity of the patient). The reason for the superior energy absorption of 16% porous NiTi is that at a given stress, it deforms to a much larger strain (Fig. 8(c)).

Finally, at a given maximum strain ε_{max}, both monolithic and 16% porous samples absorb less energy in the aged condition than in the furnace-cooled condition; this is because the furnace-cooled NiTi has higher apparent Young's modulus and plateau stress (Fig. 7(a) and (d)). Comparing the two heat-treatment conditions for the energy as a function of the maximum stress σ_{max} shows that, for the monolithic samples, the aging heat-treatment is more favorable, whereas for the 16% porous samples, there is no significant difference between the two heat-treatments.

4.3.4. Bone-replacement applications

Achieving the stiffness target range of $E_{bone} = 12$–17 GPa at the lowest possible porosity in NiTi is important, since it maximizes the implant strength, both under static and fatigue conditions, which may become limiting for long-term implantation of porous metals. From that point of view, the exceptionally high compressive stresses carried without failure by the aged, 16% porous

NiTi (>975 MPa after mechanical training, Fig. 7(d)) coupled with its unusually low apparent stiffness ($E_{app} = 15 \pm 1$ GPa) is unique among known bone-replacement materials, especially when considering the very large compressive ductility (>7%) and energy absorption (>30 MJ/m^3).

We expect the apparent Young's modulus and the superelastic parameters (yield stress, slope and extent of plateau stress, recoverable and superelastic strain, energy absorption) to be tailorable—within a certain range—by altering the material composition, heat-treatment and porosity (e.g., pore fraction, shape, connectivity and spatial distribution). These independent variables may allow custom materials to be used in a wide variety of medical (and non-medical) structural applications. However, the mechanical properties are also likely to depend sensitively on temperature. For bone-replacement implants which remain at a near-constant human body temperature (36–42 °C), this issue is less critical.

The present porous NiTi would benefit from open porosity, so as to allow bone ingrowth and mechanical anchorage between implant and bone. For current monolithic titanium implants, rounded powders are sintered on the implant surface, resulting in a highly porous surface layer [47] and this approach could be used with the current closed porosity NiTi materials as well. Alternatively, increased level of foaming will lead to opening of the porosity, as reported in titanium foams [42,43]. However, for higher porosity levels, appropriate heat-treatments (e.g., similar to the present "furnace-cooled" treatment) may be needed to insure that the apparent Young's modulus remains near the value for human compact bone.

Finally, the superelastic effect could be used to help anchor a porous NiTi implant within the receiving bone cavity. One could envision that the superelastic porous implant, deformed in compression within a holding sleeve, is pushed into the bone cavity where it expands by superelastic recovery, thus improving fixation within the bone by mechanical locking. A similar approach is used for NiTi stents, which are introduced within veins or arteries in a low profile, deformed shape, and subsequently deployed at the correct position through the superelastic effect [48,49].

5. Conclusions

Pre-alloyed, near-stoichiometric NiTi powders were densified in the presence of argon gas, resulting in a NiTi billet with <1 vol.% pores containing high-pressure argon, which were subsequently expanded at high temperature to create up to 20% internal porosity. Study of a series of porous NiTi samples led to the following main conclusions:

- Upon foaming at 1200 °C, porosity increases rapidly up to about 11% porosity and then more sluggishly up to 20% porosity, with rates increasing with initial Ar pressure. Pores are equiaxed (except when they coalesce into elongated pore agglomerates), inhomogenously distributed (due to primary NiTi powders) and unconnected to the surface.
- The Young's modulus determined by ultrasonic measurements decreases with increasing porosity, in general agreement with elastic Eshelby-based theory for closed, spherical porosity. The Young's modulus measured during uniaxial compression is significantly lower than the dynamic measurement, as a result of superelastic deformation within the linear-elastic range.
- Specimen with 0%, 5.6%, 11% and 16% porosity, in the furnace cooled or aged condition, exhibit superelasticity, while homogenization results in a normal elasto-plastic behavior with no superelasticity. For the porous specimens, a large superelastic strain of about 5.5% was recovered upon unloading from stresses of 900–1700 MPa.
- The 16% porous, aged NiTi materials exhibit a combination of mechanical properties unique among bio-compatible materials: very high strength ($\sim$1000 MPa), low apparent stiffness ($\sim$15 GPa, matching compact human bone), large compressive ductility (>7%), large recoverable strains (>6%), and high energy absorption (>30 MJ/m^3). This makes porous NiTi an excellent candidate for bone replacement applications.

Acknowledgements

References

[1] Simske SJ, Ayers RA, Bateman TA. Porous materials for bone engineering. Mater Sci Forum 1997;250:151–82.

[2] Gibson LJ, Ashby MF. Cellular solids. Cambridge: Cambridge University Press; 1997.

[3] Bobyn JD, Mortimer ES, Glassman AH, Engh CA, Miller JE, Brooks CE. Producing and avoiding stress shielding—laboratory and clinical observations of noncemented total hip-arthroplasty. Clin Orthop Rel Res 1992;274:79–96.

[4] Kienapfel H, Sprey C, Wilke A, Griss P. Implant fixation by bone ingrowth. J Arthroplast 1999;14:355–68.

[5] Urban RM, Jacobs JJ, Sumner DR, Peters CL, Voss FR, Galante JO. The bone–implant interface of femural stems with non-circumferential porous coating—a study of specimens retrieved at autopsy. J Bone Jt Surg—Am Vol A 1996;78:1068–81.

[6] Kang SB, Yoon KS, Kim JS, Nam TH, Gjunter VE. In vivo result of porous TiNi shape memory alloy: bone response and growth. Mater Trans 2002;43:1045–8.

[7] Li BY, Rong LJ, Li YY, Gjunter VE. Fabrication of cellular NiTi intermetallic compounds. J Mater Res 2000;15:10–3.

[8] Rausch G, Banhart J. Making cellular materials from metals other than aluminum. In: Degischer HP, Kriszt B, editors. Handbook of cellular metals. Weinheim: Wiley-VCH; 2002. p. 18–25.

[9] Davis NG, Teisen J, Schuh C, Dunand DC. Solid-state foaming of titanium by superplastic expansion of argon-filled pores. J Mater Res 2001;16:1508–19.

[10] Zardiackas LD, Parsell DE, Dillon LD, Mitchell DW, Nunnery LA, Poggie R. Structure, metallurgy, and mechanical properties of a porous tantalum foam. J Biomed Mater Res 2001;58:180–7.

[11] Tuukkanen J, Danilov A, Ryhanen J, Kujala S. Effect of porosity on the osteointegration and bone ingrowth of a weight-bearing nickel–titanium bone graft substitute. Biomaterials 2003;24: 4691–7.

[12] Duering TW, Pelton AR. Materials properties handbook: titanium alloys. Materials Park, OH: ASM International, The Materials Information Society; 1994.

[13] Otsuka K, Wayman CM. Shape memory materials. Cambridge: Cambridge University Press; 1998.

[14] Chu CL, Chung CY, Lin PH, Wang SD. Fabrication of porous NiTi shape memory alloy for hard tissue implants by combustion synthesis. Mater Sci Eng A 2004;366:114–9.

[15] Li BY, Rong LJ, Li YY, Gjunter VE. An investigation of the synthesis of Ti–50at.pct Ni alloys through combustion synthesis and conventional powder sintering. Metall Mater Trans A 2000;31:1867–71.

[16] Oppenheimer SM, O'Dwyer JG, Dunand DC. Porous, superelastic NiTi produced by powder-metallurgy. TMS Lett 2004;1:93–4.

[17] Li BY, Rong LJ, Li YY. Porous NiTi alloy prepared from elemental powder sintering. J Mater Res 1998;13:2847–51.

[18] Li BY, Rong LJ, Li YY. Stress–strain behavior of porous Ni–Ti shape memory intermetallics synthesized from powder sintering. Intermetallics 2000;8:643–6.

[19] Li BY, Rong LJ, Li YY, Gjunter VE. A recent development in producing porous Ni–Ti shape memory alloys. Intermetallics 2000;8:881–4.

[20] Li BY, Rong LJ, Li YY. Microstructure and superelasticity of porous NiTi alloy. Sci China Series E—Technol Sci 1999;42:94–9.

[21] Biswas A. Porous NiTi by thermal explosion mode of SHS: processing, mechanism and generation of single phase microstructure. Acta Mater 2005;53:1415–25.

[22] Li YH, Rong LJ, Li YY, Gunther VE. Influence of Ti powder characteristics on combustion synthesis of porous NiTi alloy. J Mater Sci Technol 2002;18:248–50.

[23] Li BY, Rong LJ, Li YY, Gjunter VE. Synthesis of porous Ni–Ti shape-memory alloys by self-propagating high-temperature synthesis: reaction mechanism and anisotropy in pore structure. Acta Mater 2000;48:3895–904.

[24] Chu CL, Chung CY, Lin PH. Influence of solution treatment on the compressive properties of porous NiTi shape memory alloy of 53.4 vol.% fabricated by combustion synthesis. J Mater Sci 2004;39:4949–51.

[25] Yuan B, Chung CY, Zhu M. Microstructure and martensitic transformation behavior of porous NiTi shape memory alloy prepared by hot isostatic pressing processing. Mater Sci Eng A 2004;382:181–7.

[26] Chung CY, Chu CL, Wang SD. Porous TiNi shape memory alloy with high strength fabricated by self-propagating high-temperature synthesis. Mater Lett 2004;58:1683–6.

[27] Kim JS, Kang JH, Kang SB, Yoon KS, Kwon YS. Porous TiNi biomaterial by self-propagating high-temperature synthesis. Adv Eng Mater 2004;6:403–6.

[28] Zhu SL, Yang XJ, Hu F, Deng SH, Cui ZD. Processing of porous TiNi shape memory alloy from elemental powders by Ar-sintering. Mater Lett 2004;58:2369–73.

[29] Dunand DC. Reactive synthesis of aluminide intermetallics. Mater Manuf Proc 1995;10:373–403.

[30] Kim JS, Kang JH, Kang SB, Yoon KS, Kwon YS. Porous TiNi biomaterial produced by self-propagating high-temperature synthesis: pore structure, mechanical properties and application. Mater Sci Forum 2004;449:1097–100.

[31] Li BY, Rong LJ, Gjunter VE, Li YY. Porous Ni–Ti shape memory alloys produced by two different methods. Z Metallkd 2000;91:291–5.

[32] Lagoudas DC, Vandygriff EL. Processing and characterization of NiTi porous SMA by elevated pressure sintering. J Intell Mater Syst Struct 2002;13:837–50.

[33] Entchev PB, Lagoudas DC. Modeling of transformation-induced plasticity and its effect on the behavior of porous shape memory alloys. Part II: Porous SMA response. Mech Mater 2004;36: 893–913.

[34] Zhao Y, Taya M, Kang Y, Kawasaki A. Compression behavior of porous NiTi shape memory alloy. Acta Mater 2005;53:337–343.

[35] Queheillalt DT, Choi BW, Schwartz DS, Wadley HNG. Creep expansion of porous Ti–6Al–4V sandwich structures. Metall Mater Trans A 2000;31:261–73.

[36] Murray NGD, Schuh C, Dunand DC. Solid-state foaming of titanium by hydrogen-induced internal stress superplasticity. Scr Mater 2003;49:879–83.

[37] Kearns MW, Blenkinsop PA, Barber AC, Farthing TW. Manufacture of a novel porous metal. Int J Powder Metall 1988;24: 59–64.

[38] Vaidyanathan R, Bourke MAM, Dunand DC. Texture, strain, and phase-fraction measurements during mechanical cycling in superelastic NiTi. Metall Mater Trans A 2001;32:777–86.

[39] Bourke MAM, Vaidyanathan R, Dunand DC. Neutron diffraction measurement of stress-induced transformation in superelastic NiTi. Appl Phys Lett 1996;69:2477–9.

[40] Vaidyanathan R, Bourke MAM, Dunand DC. Phase fraction, texture and strain evolution in superelastic NiTi and NiTi–TiC composites investigated by neutron diffraction. Acta Mater 1999;47:3353–66.

[41] Vaidyanathan R, Bourke MAM, Dunand DC. Analysis of neutron diffraction spectra acquired in situ during stress-induced transformations in superelastic NiTi. J Appl Phys 1999;86:3020–9.

[42] Murray NGD, Dunand DC. Effect of thermal history on the superplastic expansion of argon-filled pores in titanium: Part I Kinetics and microstructure. Acta Mater 2004;52:2269–78.

[43] Murray NGD, Dunand DC. Microstructure evolution during solid-state foaming of titanium. Compos Sci Technol 2003;63: 2311–6.

[44] Murray NGD, Dunand DC. Effect of thermal history on the superplastic expansion of argon-filled pores in titanium: Part II Modeling of kinetics. Acta Mater 2004;52:2279–91.

[45] Davis NG. PhD Thesis. Northwestern University 2002.

[46] Li H, Oppenheimer SM, Stupp SI, Dunand DC, Brinson LC. Effects of pore morphology and bone ingrowth on mechanical properties of microporous titanium as an orthopaedic implant material. Mater Trans 2004;45:1124–31.

[47] Soballe K et al. Fixation of titanium and hydroxyapatite-coated implants in arthritic osteopenic bone. J Arthroplast 1991;6: 307–17.

[48] Stoeckel D. Nitinol medical devices and implants. Minim Invas Therapy Allied Technol 2000;9:81–8.

[49] Stoeckel D, Pelton A, Duering T. Self-expanding nitinol stents: material and design considerations. Eur Radiol 2004;14:292–301.